

Revealing the dynamic responses of Pb under shock loading based on DFT-accuracy machine learning potential

Enze Hou(侯恩则), Xiaoyang Wang(王啸洋), and Han Wang(王涵)
Citation: Chin. Phys. B, 2026, 35 (**1**): 018701. DOI: 10.1088/1674-1056/ae1726
http://cpb.iphy.ac.cn; http://iopscience.iop.org/cpb

What follows is a list of articles you may be interested in

Reconfiguration of B-DNA structure induced by ethanol

Yue Huang(黄悦), Yipeng Chen(陈以鹏), Jing Li(李静), Rongri Tan(谈荣日), and Huanhuan Qiu(邱环环)
Chin. Phys. B, 2025, 34 (**8**): 088707. DOI: 10.1088/1674-1056/adbed9

Molecular simulation study on phase separation of immunoglobulin G

Lv-Meng Hu(胡吕梦), Yuan-Qiang Chen(陈远强), Hong-Ming Ding(丁泓铭), and Yu-Qiang Ma(马余强)
Chin. Phys. B, 2025, 34 (**8**): 088701. DOI: 10.1088/1674-1056/add50b

Depolymerization mechanism of microtubule revealed by nucleotide-dependent changes of longitudinal and lateral interactions

Bingbing Zhang(张冰冰), Ziling Huo(霍子玲), Jiaxi Li(李佳希), Jingyu Qin(覃静宇), and Yizhao Geng(耿轶钊)
Chin. Phys. B, 2025, 34 (**6**): 068702. DOI: 10.1088/1674-1056/adc369

Effects of palmitoylation on membrane protein partitioning into lipid domains in model cellular membranes

Shishi Wu(吴施施) and Qing Liang(梁清)
Chin. Phys. B, 2025, 34 (**5**): 058701. DOI: 10.1088/1674-1056/adbee9

Factors resisting protein adsorption on hydrophilic/hydrophobic self-assembled monolayers terminated with hydrophilic hydroxyl groups

Dangxin Mao(毛党新), Yuan-Yan Wu(吴园燕), and Yusong Tu(涂育松)
Chin. Phys. B, 2024, 33 (**6**): 068701. DOI: 10.1088/1674-1056/ad39ca

---

SPECIAL TOPIC — AI + Physical Science

Revealing the dynamic responses of Pb under shock loading based on DFT-accuracy machine learning potential

Enze Hou(侯恩则)[1,2], Xiaoyang Wang(王啸洋)[3], and Han Wang(王涵)[3,4,†]

[1] *Institute of Applied Physics and Computational Mathematics, Beijing* 100094, *China*
[2] *Graduate School of China Academy of Engineering Physics, Beijing* 100088, *China*
[3] *Laboratory of Computational Physics, Institute of Applied Physics and Computational Mathematics, Beijing* 100094, *China*
[4] *HEDPS, CAPT, College of Engineering and School of Physics, Peking University, Beijing* 100871, *China*

(Received 31 July 2025; revised manuscript received 22 October 2025; accepted manuscript online 24 October 2025)

Lead (Pb) is a typical low-melting-point ductile metal and serves as an important model material in the study of dynamic responses. Under shock-wave loading, its dynamic mechanical behavior comprises two key phenomena: plastic deformation and shock-induced phase transitions. The underlying mechanisms of these processes are still poorly understood. Revealing these mechanisms remains challenging for experimental approaches. Non-equilibrium molecular dynamics (NEMD) simulations are an alternative theoretical tool for studying dynamic responses, as they capture atomic-scale mechanisms such as defect evolution and deformation pathways. However, due to the limited accuracy of empirical interatomic potentials, the reliability of previous NEMD studies has been questioned. Using our newly developed machine learning potential for Pb–Sn alloys, we revisited the microstructural evolution in response to shock loading under various shock orientations. The results reveal that shock loading along the [001] orientation of Pb exhibits a fast, reversible, and massive phase transition and stacking-fault evolution. The behavior of Pb differs from previous studies by the absence of twinning during plastic deformation. Loading along the [011] orientation leads to slow, irreversible plastic deformation, and a localized FCC–BCC phase transition in the Pitsch orientation relationship. This study provides crucial theoretical insights into the dynamic mechanical response of Pb, offering a theoretical input for understanding the microstructure-performance relationship under extreme conditions.

Keywords: interatomic potentials, molecular dynamics, shock impacts, machine learning

PACS: 87.10.Tf, 34.20.Cf, 62.50.Ef, 84.35.+i

DOI: 10.1088/1674-1056/ae1726 **CSTR:** 32038.14.CPB.ae1726

1. Introduction

As a typical group IV metal, lead (Pb) has a low ambient-pressure melting point of approximately 600 K. Pb has a complex pressure–temperature phase diagram. At ambient pressure, Pb has a ductile face-centered cubic (FCC) phase and transforms to the hexagonal close-packed (HCP) phase at $\sim$ 13 GPa.[1] At $\sim$ 109 GPa, Pb transforms to the body-centered cubic (BCC) phase. Both the FCC–HCP and HCP–BCC transitions are considered sluggish, weakly first-order transformations with minimal density changes.[2] Under shock loading, the shock Hugoniot curve passes through all three phases, leading to complex dynamic behaviors, including plastic deformation[3] and solid-state phase transitions[4] at high strain rates. These unique properties make Pb a key model material for studying material responses under dynamic loading.

Experimental studies of the dynamic response of Pb have focused primarily on macroscopic dynamic fracturing. For example, Chen *et al.*[5] studied the mass and density distribution of fragmented Pb during micro-spallation. Antipov *et al.*[6] investigated fragments of explosively shocked Pb and quantitatively determined ejecta, spallation, and undamaged regions. However, due to the lack of experimental approaches for characterizing microstructures under extreme conditions, atomistic-scale processes under dynamic loading, such as defect evolution, phase transitions, and void nucleation, remain poorly understood. Non-equilibrium molecular dynamics (NEMD) simulations serve as a powerful alternative tool for investigating dynamic responses under shock loading. For example, Xiang *et al.*[7–9] investigated shock-induced spallation of nanocrystalline Pb; Wang *et al.*[10] explored the spall response of release-melted Pb; and Mayer *et al.*[11] simulated the sensitivity of spall strength to strain rates. These simulations complement and validate experimental findings.

Importantly, NEMD simulations can resolve microstructural evolution during the short period of dynamic loading prior to fracture, which is critical for a comprehensive understanding of the microstructure–performance relationship under extreme conditions. For example, Li *et al.*[12] studied the atomistic processes of shock-induced plasticity, which were found to operate via slip and deformation twinning. They

†Corresponding author. E-mail: wang_han@iapcm.ac.cn

© 2026 Chinese Physical Society and IOP Publishing Ltd. All rights, including for text and data mining, AI training, and similar technologies, are reserved.

pointed out that twins formed due to mutual impediments of slip and cross-slip may act as nucleation sites for subsequent FCC–HCP phase transitions. In addition, BCC structures were observed to form along the Bain path and mostly returned to FCC upon further relaxation within tens of picoseconds.

It is worth noting that most existing NEMD studies utilize empirical interatomic potentials, which are highly efficient formalisms employing fixed functional forms and a limited number of parameters fitted to selected material properties. A well-known issue with empirical potentials is that they can hardly describe multiple phases accurately over a wide range of thermodynamic conditions. Meanwhile, their transferability is usually insufficient for accurately simulating a wide variety of defects. For instance, the study by Li *et al.*[12] employed the embedded atom method (EAM) potential developed by Wang *et al.*,[13] which accurately reproduces Pb's Hugoniot curve but underestimates melting points above 40 GPa. Moreover, in our separate tests of this EAM potential, the formation energy of deformation twinning along the (111) plane is negative, which could lead to overestimation or unphysical formation of twins during MD simulations. The reliability of simulation results could therefore be compromised by inaccuracies in the empirical potential.

For Pb, first-principles calculations based on density functional theory (DFT) have been extensively applied to investigate its phase structures and phase diagram. For instance, Liu *et al.*[14] and Cui *et al.*[15] computed the critical pressures for phase transitions in Pb, with the calculated FCC–HCP and HCP–BCC transition pressures showing good agreement with experiments.[1,2] In addition, Cricchio *et al.*[16] used *ab initio* molecular dynamics (AIMD) to determine the melting curve of Pb as a function of pressure, which also aligns well with experimental data.[17] Furthermore, Yu *et al.*[18] calculated the surface energy, which is consistent with experimental measurements.[19] These agreements demonstrate the high reliability of DFT in predicting the properties of Pb. However, AIMD cannot be directly applied to simulate dynamic mechanical responses, as the computational complexity of DFT scales cubically with the number of electrons, making such simulations prohibitively expensive for large systems and long timescales.

Fortunately, recent developments in machine-learning potentials (MLPs)[20–32] have revolutionized atomic-scale simulations by offering both high accuracy and computational efficiency in research fields such as perovskites,[33] nuclear materials,[34] superconductors,[35] high-energy-density materials,[36] high-pressure water phases,[37,38] and atmospheres of gas giant planets.[39] MLPs have also been widely employed in non-equilibrium dynamic simulations. For instance, Gao *et al.*[40] investigated ultrafast laser-induced melting of copper nanofilms using an MLP; Zeng *et al.*[41] examined liquid iron under extreme conditions; Liu *et al.*[42] studied the spallation behavior of p-phenylene terephthalamide crystals; D'Souza *et al.*[43] explored the behavior of deuterium under shock loading; Pan *et al.*[44] analyzed shock compression pathways in pyrite silica; and Zeng *et al.*[45] researched shock-induced phase transitions in solid iron at high pressures. These examples collectively demonstrate the applicability and reliability of MLPs in simulating dynamic material responses. We recently developed a MLP named DP-PbSn,[46] tailored for Pb–Sn alloys with up to 30 at.% Sn.

With the aid of the non-von Neumann molecular dynamics (NVNMD) architecture,[47] this potential can access large-scale NEMD simulations involving millions of atoms with first-principles accuracy over a wide thermodynamic range (0–5000 K, 0–100 GPa). In this work, we employ this potential in NEMD simulations to revisit atomistic processes in the dynamic response of Pb, including shock-induced plasticity and the evolution of the BCC phase during shock loading. Meanwhile, the anisotropy of shock-induced plastic deformation and phase transformation in Pb is investigated. The findings of this study may provide new mechanistic insights into the dynamic mechanical response of Pb. Meanwhile, the techniques used here can be applied to investigate dynamic processes in other materials.

2. Methods

In this section, we first briefly introduce the MLP, then present the molecular dynamics setups employed in this study.

2.1. The MLP: DP-PbSn

The MLP employed in this study, namely, DP-PbSn, was developed based on the DeepMD-Kit[28,48] framework. This potential was trained on a dataset comprising over 8217 configurations, covering a thermodynamic range of 0–100 GPa and 0–5000 K. The dataset encompassed molecular dynamics trajectories of BCC, FCC, HCP, and liquid phases of Pb–Sn alloy, sampled both during the evolution toward equilibrium and after equilibrium under the target thermodynamic conditions. These phases are experienced by the material along the shock Hugoniot during compression. Moreover, the structures of mono-vacancies and free surfaces were included in the training dataset, which enhances the reliability of the potential in describing fracture nucleation. For dataset generation, the DFT calculations utilized a plane-wave basis set implemented in the ABACUS code.[49,50] The Perdew–Burke–Ernzerhof (PBE) exchange-correlation functional within the generalized gradient approximation (GGA)[51] was used. An energy cutoff of 100 Ry and a Monkhorst–Pack k-point sampling grid spacing of 0.15 Å^{-1} were selected. The optimized norm-conserving Vanderbilt

(ONCV) pseudopotentials[52] from PseudoDojo[53,54] were employed.

The MLP achieved a testing RMSE on an independent test set of 2.27 meV/atom, 40.6 meV/Å, and 25.8 meV/atom for energy, force, and virial tensor, respectively. The detailed DP-PbSn characterization results are presented in Ref. [46].

The Hugoniot curve of Pb calculated using NEMD simulations is presented in Fig. 1. While the pressure–density (P–ρ) relationship along the Hugoniot predicted by DP-PbSn follows the general trend of the experimental data (Fig. 1(a)), it exhibits a nearly constant shift toward lower pressure. The observed deviation between the calculated Hugoniot curve and experimental data likely stems from systematic errors in DFT calculations when compared with experimental results. As evidenced by the equation of state reported in Ref. [10], DFT calculations may consistently underestimate the pressure relative to experimental measurements at equivalent volumes. This systematic underestimation is consistent with the discrepancies shown in our results. The particle velocity–wave velocity (v_p–v_s) relationship obtained with DP-PbSn is shown in Fig. 1(b), demonstrating near-linear behavior that closely matches the experimental measurements.[55] These Hugoniot curve results further validate the applicability of DP-PbSn for investigating dynamic mechanical responses.

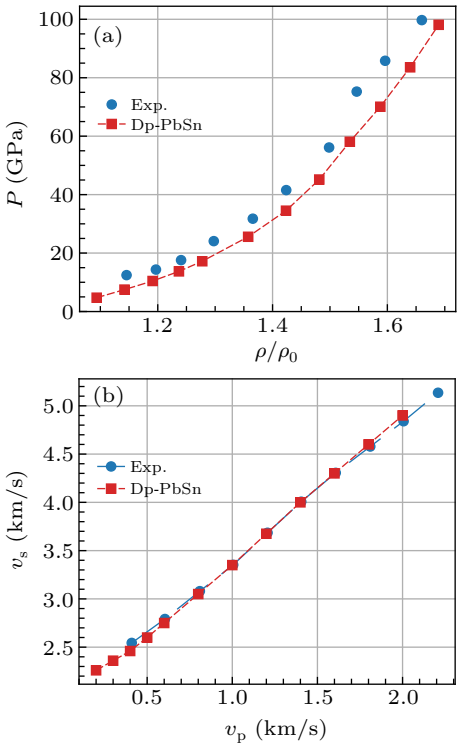


Fig. 1. The Hugoniot curve predicted by DP-PbSn. (a) The pressure–density relationship compared with experimental results from Ref. [55]. (b) The shock-wave velocity–piston velocity relationship compared with experimental results.[55] These results were reproduced from Ref. [46] with permission from the authors.

2.2. Molecular dynamics setup

We performed NEMD simulations on FCC Pb samples with dimensions of approximately 100 Å × 100 Å × 1000 Å along the x, y, and z axes. The samples comprised 320000 atoms. The simulation cell size was sufficient to capture the dynamic processes from shock compression to the onset of dynamic fracture, while also representing a practical compromise given the substantial computational cost associated with the MLP. Prior to dynamic loading, the sample was equilibrated at 300 K and zero pressure using the NPT ensemble for 50 ps. Periodic boundary conditions were applied along all dimensions during the equilibrium simulation.

In the non-equilibrium simulation, dynamic loading was applied via a piston at the lower z boundary of the sample, with a controlled particle velocity v_p ranging from 0.2 km/s to 1.4 km/s, generating a compressive shock wave that propagated toward the upper z boundary.[56] An NVE ensemble was applied to the system throughout the NEMD simulations. Periodic boundary conditions were maintained in the x and y dimensions, while the boundary condition along the z dimension was set to free. The piston was removed immediately when the shock wave reached the upper z boundary. As a result, a release wave from the lower z boundary and a rarefaction wave reflected from the upper z boundary were initiated simultaneously. During the NEMD simulations, we implemented an adaptive time step ranging from 0.001 fs to 1 fs, ensuring that the maximum atomic displacement within any single time step did not exceed 0.1 Å. The use of an adaptive time step effectively balanced the temporal resolution required to capture rapidly evolving dynamical processes against the computational cost associated with MLPs.

The equilibrium and NEMD simulations were implemented using the LAMMPS package.[57] The material properties were evaluated by analyzing thin slices along the z direction of the system. The width of each slice was 2.0 Å. Within each slice, we computed the per-atom velocity (v_i), pressure, shear stress, and local temperature. The shear stress was calculated as

$$\tau = \frac{1}{2}\left[\sigma_{zz} - \frac{1}{2}\left(\sigma_{xx} + \sigma_{yy}\right)\right], \tag{1}$$

where σ is the stress tensor of each atom. The local temperature was calculated as

$$T = \frac{1}{3Nk_b}\sum_{i=1}^{N} m_i\left[v_{i,x}^2 + v_{i,y}^2 + (v_{i,z} - v_{\mathrm{com},z})^2\right], \tag{2}$$

where $v_{\mathrm{com},z}$ is the center-of-mass velocity of each slice along the z direction, which was properly removed for temperature evaluation.

The crystal structure in the NEMD snapshots was primarily determined via polyhedral template matching (PTM) analysis.[58] Visualization of the snapshots was performed using the OVITO software.[59]

3. Results

3.1. Shock along [001] direction

Figures 2(a) and 2(b) present the spatial distributions of pressure and temperature along the z direction at a representative simulation time after shock loading along the [001] direction. For all simulated v_p values, the compressed region exhibits a relatively uniform pressure plateau behind the shock-wave front. The temperature profiles show peak values at the shock-wave front and gradually converge to a plateau. The maximum (P,T) condition in our simulations was (58 GPa, 4000 K), which lies within the thermodynamic range covered by DP-PbSn.

Figure 3 presents the distribution of shear stress and the corresponding snapshots during shock loading. The shear stress profiles effectively reveal the microstructural evolution under compression. At $v_p = 0.2$ km/s, Pb undergoes neither plastic deformation nor solid-phase transformation, maintaining an FCC structure that exhibits characteristically high shear stress. With increasing v_p, the shear stress within the compressed region is significantly relaxed, accompanied by plastic deformation. A notable phenomenon emerges in which atoms near the shock front are transiently identified as having a BCC structure. However, these metastable BCC structures rapidly degenerate into deformed FCC phases within a few picoseconds. Stripe-like regions identified as HCP structures emerge at approximately 45° to the shock propagation direction, corresponding to stacking faults within the FCC phase. This transient BCC formation and subsequent reversion behavior has been previously reported by Li *et al.*[1,2]

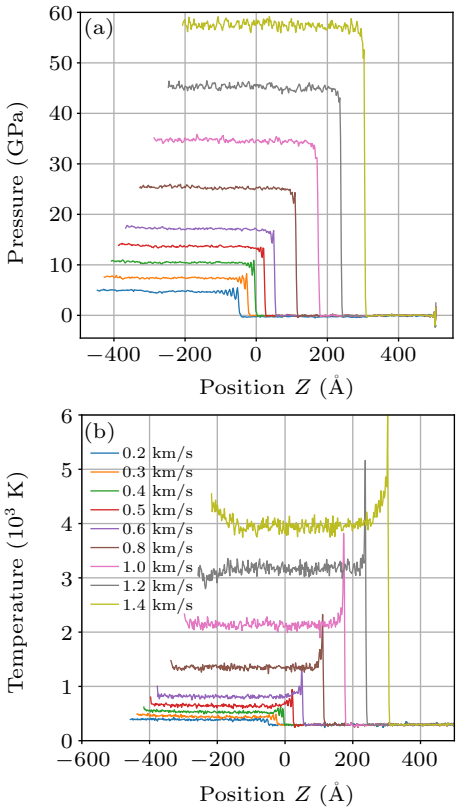


Fig. 2. Spatial distributions of thermodynamic quantities during loading along the [001] direction at 20 ps after piston loading. (a) Pressure distribution. (b) Local temperature distribution.

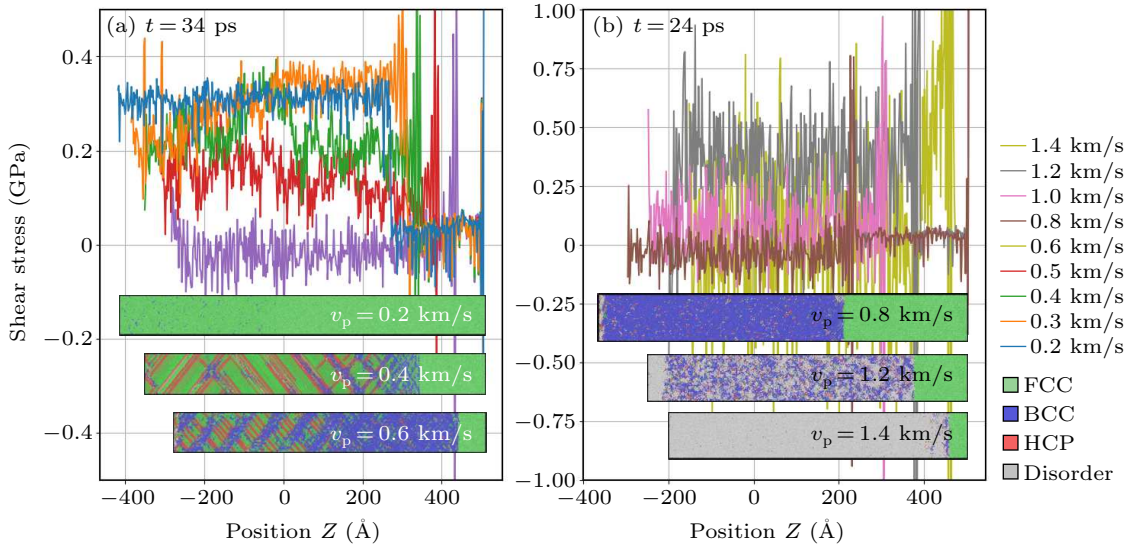


Fig. 3. Distribution of shear stress and representative snapshots during loading along the [001] direction. (a) 0.2 km/s $\leq v_p \leq$ 0.6 km/s at 34 ps after piston loading. (b) 0.8 km/s $\leq v_p \leq$ 1.4 km/s at 24 ps after piston loading.

The major difference between the results of this study and those of Li *et al.*[12] lies in the activated deformation mechanisms during shock-induced plasticity. In this study, only slip was activated during [001] loading. However, in the study by Li *et al.*,[12] not only slip but also twinning was operative during plastic deformation, which was possibly caused by the unphysical negative twin formation energy (−0.51 meV/Å^2) predicted by the EAM potential. By contrast, DP-PbSn predicted a twin formation energy of nearly 1.0 meV/Å^2, which underestimates the DFT value of 3.3 meV/Å^2. Twinning structures

were not included in the dataset of DP-PbSn. However, even with this underestimation, twinning was still not operative during shock compression in our simulations.

Further increasing v_p drove the P–T conditions in the compressed region closer to the BCC phase region of the equilibrium phase diagram. Consequently, the stability of shock-induced BCC structures was enhanced. At $v_p = 0.6$ km/s, the proportion of BCC regions within the shock wave exceeded that of the deformed FCC phase, accompanied by near-zero shear stress in the compressed material. When v_p was further increased to 0.8 km/s, nearly all atoms within the compressed regions were identified as BCC structures. The reversion to FCC structures completely disappeared. The shear stress distribution remained approximately zero, demonstrating that both the FCC–BCC phase transformation and plastic deformation under shock loading effectively relaxed the shear stress.

Interestingly, although the compressed region at $v_p = 0.8$ km/s became predominantly BCC structured, the corresponding thermodynamic conditions did not enter the equilibrium BCC phase region. This apparent contradiction stems from the unique FCC–BCC transition pathway under shock loading along the [001] direction. The Bain path[60] for the FCC–BCC transformation requires substantial compression along the [001] direction and involves a tremendously high energy barrier under near-equilibrium conditions. However, during dynamic processes, shock compression along the [001] orientation drives FCC deformation that aligns with the Bain path, enabling a forced transformation from FCC to BCC within picoseconds. Once formed, the BCC phase is maintained if it is dynamically stable at the attained (P,T) conditions, or reverts to a deformed FCC structure if the (P,T) conditions are too low.

Further increasing v_p led to a gradual diminution of the shock-induced BCC phase. As shown in Fig. 3(b), at $v_p = 1.2$ km/s, atoms in the compressed regions became increasingly disordered. When v_p reached 1.4 km/s, almost all atoms within the shock front became disordered. The corresponding thermodynamic conditions (58 GPa, 4000 K, as shown in Fig. 2) exceeded the melting line in the equilibrium phase diagram,[4] indicating shock-induced melting.

The above processes exhibit a typical phase evolution from FCC to BCC followed by shock-induced melting. No FCC–HCP phase transformation was observed. It is well established that this phase transformation is sluggish even on experimental timescales.[2] Therefore, within the short timescales accessible to NEMD simulations, substantial nucleation of the HCP phase is unlikely. Moreover, the FCC–HCP phase transformation is known to proceed via the sequential glide of Shockley partial dislocations on every other close-packed {111} plane in the FCC lattice.[61] This mechanism requires a higher dislocation density than that observed in our simulations, which explains the absence of HCP nucleation in this study. This discrepancy is likely attributable to the use of a perfect single crystal in the molecular dynamics simulations. In real materials, the presence of defects across multiple length scales can act as dislocation sources under rapid deformation, potentially generating a higher dislocation density and thereby initiating HCP nucleation.

Upon reaching the free surface, the shock wave generated a rarefaction wave that propagated in the opposite direction. At the same time, the piston was unloaded, leading to the generation of a release wave. Figure 4 illustrates the distributions of pressure and temperature together with representative snapshots during the unloading process. Following the rarefaction and release waves, the temperature and pressure in the unloaded region gradually decreased. At $v_p \leq 0.8$ km/s, the unloaded region predominantly retained an FCC structure. Stacking faults and the BCC phase in most of the unloaded region disappeared. The reversion from BCC to FCC during unloading followed the reverse Bain path, wherein the BCC lattice underwent significant uniaxial tensile deformation along its [001] direction to reform the FCC phase. At $v_p \geq 1.0$ km/s, the unloaded region exhibited a disordered phase rather than an FCC phase, demonstrating characteristic features of release melting.

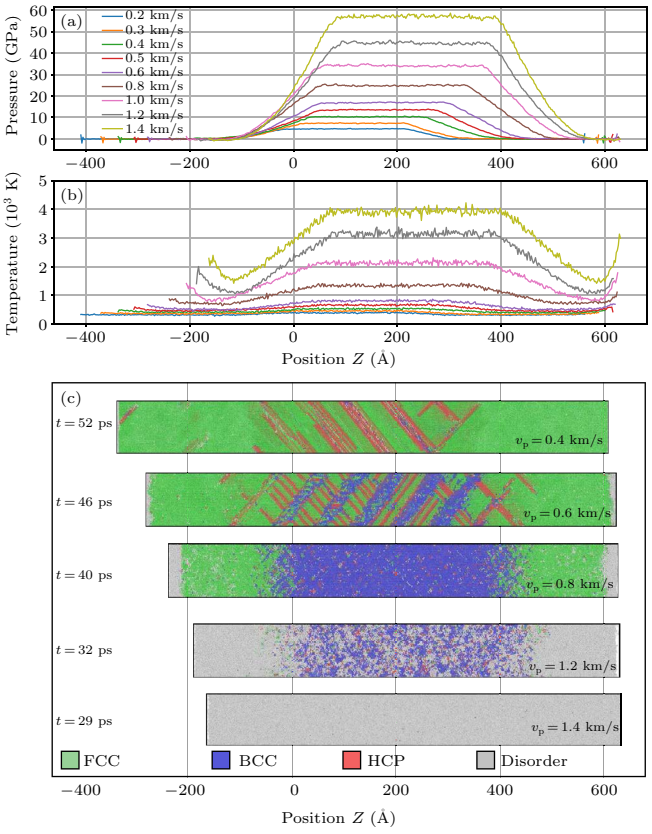


Fig. 4. (a) Distribution of pressure during [001] unloading. (b) Distribution of temperature during [001] unloading. (c) Snapshots at representative simulation times after piston loading.

3.2. Shock along [011] direction

Shock loading along the [001] direction induces an FCC–BCC transition with deformation consistent with the Bain path. When this consistency is not satisfied, FCC–BCC transition behavior is expected to differ. Moreover, when loading along other orientations, the activated slip plane may not lie perfectly at 45° to the shock propagation direction, where the shear stress is maximal. Thus, anisotropy in Pb's shock-induced plasticity and phase transition is expected. To further investigate this anisotropy, additional simulations were conducted with piston loading along the [011] orientation.

Figure 5 shows the pressure and temperature distributions during shock loading along the [011] direction. Compared with loading along the [001] orientation, the compressed region under [011] loading exhibits a more complex thermodynamic state evolution.

In the velocity range of 0.3 km/s $\leq v_{\mathrm{p}} \leq$ 1.0 km/s, the pressure in the compressed region undergoes a relaxation period before reaching its plateau value. Compared with the [001] loading cases, these relaxations are significantly slower. The temperature within the compressed region exhibits a distinct gradient, indicating that the compressed material does not immediately achieve a Hugoniot equilibrium state upon compression, but undergoes complex evolution. At $v_{\mathrm{p}} \geq 1.2$ km/s, the evolution of the (P,T) distribution reproduces its behavior under the [001] loading case. The pressure and temperature reach their plateaus immediately after compression.

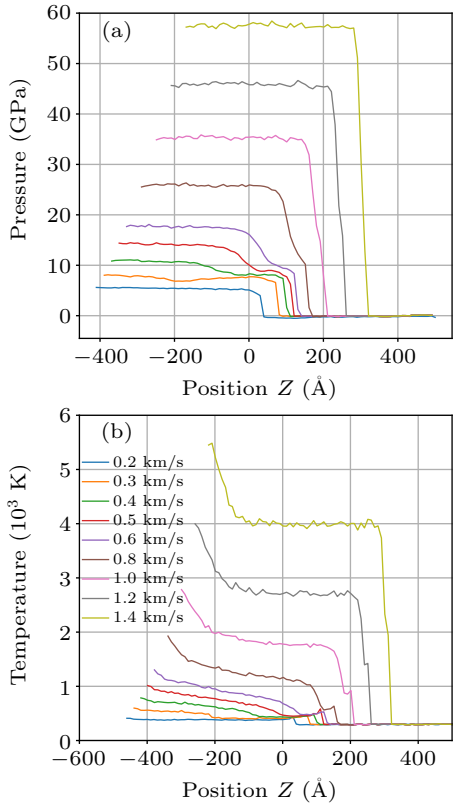


Fig. 5. Spatial distributions of thermodynamic quantities during loading along the [011] direction at 20 ps after piston loading. (a) Pressure distribution. (b) Local temperature distribution.

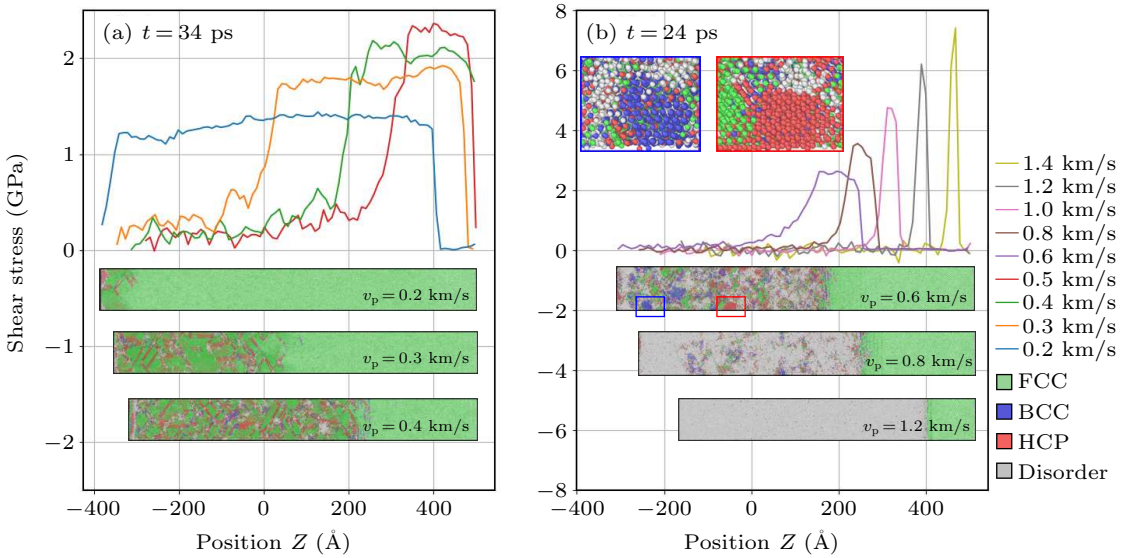


Fig. 6. Distributions of shear stress and representative snapshots during loading along the [011] direction at 20 ps after piston loading. (a) 0.2 km/s $\leq v_{\mathrm{p}} \leq$ 0.4 km/s at 34 ps after piston loading. (b) 0.6 km/s $\leq v_{\mathrm{p}} \leq$ 1.4 km/s at 24 ps after piston loading. The blue and red rectangles mark the regions where the bulk BCC and HCP phases are formed.

The shear stress distributions, along with representative snapshots of NEMD simulations for [011] loading at various v_{p}, are shown in Fig. 6. At 0.2 km/s $\leq v_{\mathrm{p}} \leq$ 0.4 km/s (Fig. 6(a)), stacking fault structures emerged along 60° orientations to the shock wave propagation direction. When v_{p} was further increased to 0.6 km/s (Fig. 6(b)), the stacking fault structures became less prevalent; instead, bulk HCP-phase (red rectangles in Fig. 6(b)) and bulk BCC-phase (blue rectangles in Fig. 6(b)) domains appeared in the compressed region. Meanwhile, the proportion of disordered structures showed a marked increase. With further increases in v_{p}, the proportion of disordered structures within the shock wave continued to

grow. When $v_p \geq 1.2$ km/s, the compressed region became almost entirely disordered. Meanwhile, the shear stress became nearly zero in the compressed region, indicating clear signatures of shock-induced melting.

The pressure and temperature distributions, together with representative snapshots during unloading along the [011] direction, are shown in Fig. 7. Pb exhibits significantly different behavior during [011] unloading compared to [001] unloading. The key difference lies in the distribution of stacking faults. As shown in Figs. 7(a) and 7(b), while the temperature and pressure gradually decay in the released region, the stacking faults generated during the loading stage were not instantly eliminated upon unloading. For example, as shown in Fig. 7(c), the unloaded region at $v_p = 0.3$ km/s, 0.4 km/s, and 0.6 km/s retains a substantial density of such plastic deformation defects identified as layered HCP structures, although the corresponding pressure has already decayed to zero. At $v_p \geq 0.8$ km/s, atoms in the unloaded region are identified as disordered structures, showing pronounced characteristics of release melting.

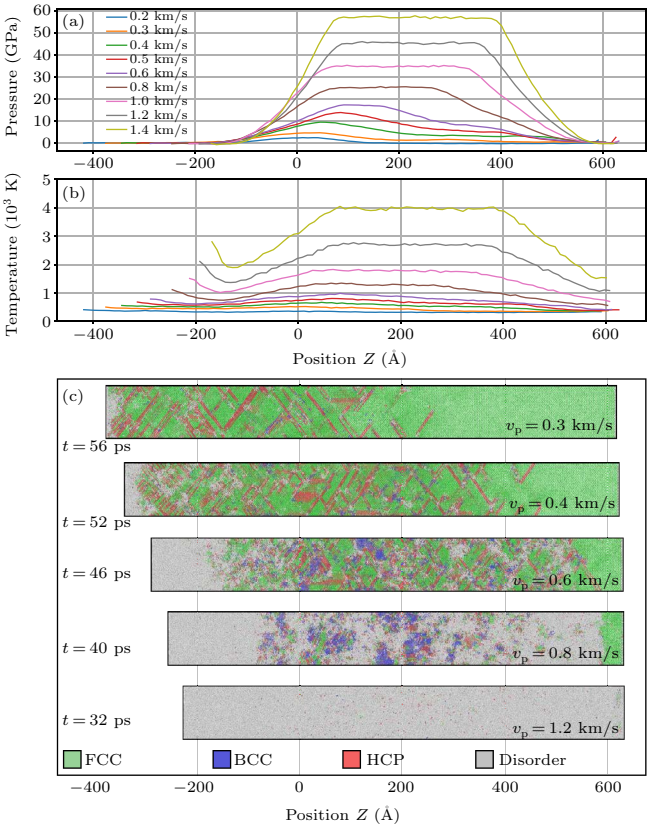


Fig. 7. (a) Pressure distribution during [011] unloading. (b) Temperature distribution during [011] unloading. (c) Snapshots at representative simulation times after piston loading.

The anisotropy of plastic deformation can be explained by the variations in the Schmid factor of the activated slip systems. In [001] loading, the activated slip systems are $[011]/(1\bar{1}1)$ and $[0\bar{1}1]/(111)$. Under uniaxial compression and tension, these slip systems exhibit the maximum Schmid factor of 0.5. This indicates that these slip systems are subjected to the maximum resolved shear stress from the applied load, facilitating their activation. However, in [011] loading, the two primarily activated slip systems are $[110]/(1\bar{1}1)$ and $[\bar{1}10]/(111)$. The Schmid factors of these slip systems are 0.433, which reduces the resolved shear stresses on them.

The anisotropy of shock-induced FCC–BCC phase transformation manifests not only in the proportion of the phase transition region but also in the crystallographic orientation relationships. The FCC and BCC phases under [001] shock loading are shown in Figs. 8(a) and 8(b), respectively, exhibiting the orientation relationship: $[001]_{FCC} \| [001]_{BCC}$; $[100]_{FCC} \| [110]_{BCC}$. This orientation relationship is typical of the well-known Bain path. However, as shown in Figs. 8(c) and 8(d), the FCC and BCC phases under [011] loading exhibit a distinct orientation relationship, approximated by $[110]_{FCC} \| [111]_{BCC}$ and $[100]_{FCC} \| [110]_{BCC}$, which agrees with the orientation relationship discovered by Pitsch.[62] Nevertheless, the NEMD simulations do not provide further insight into the detailed transformation pathways of these processes.

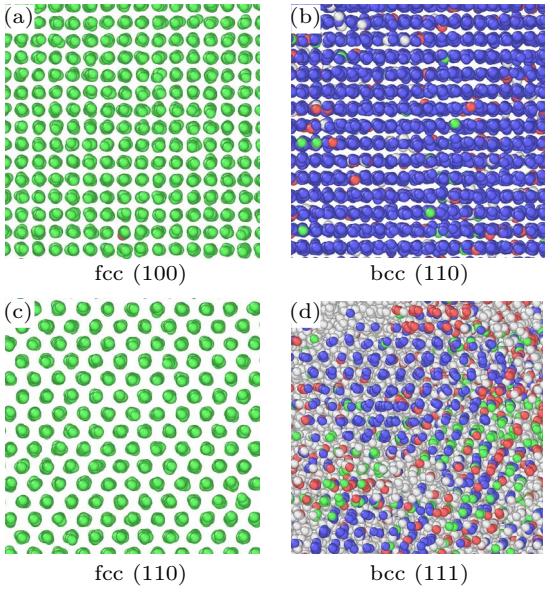


Fig. 8. Orientation relationships during dynamic loading. In [001] loading, the (100) plane of the initial FCC phase shown in panel (a) is aligned with the (110) plane in the BCC phase in the compressed region shown in panel (b). In [011] loading, the (110) plane of the initial FCC phase shown in panel (c) is aligned with the (111) plane in the BCC phase in the compressed region shown in panel (d).

4. Conclusion

To elucidate the atomistic-scale processes governing the microstructure evolution of Pb in response to shock loading, we employed a high-accuracy MLP for Pb–Sn alloys to investigate shock-induced plasticity, phase transformations, melting, and defect evolution during loading-unloading processes under shock impact along both [001] and [011] directions. The principal findings are as follows:

1. Shock plasticity exhibits pronounced anisotropy. Under [001] loading, rapid stacking fault formation occurs, which is subsequently eliminated during unloading. In contrast,

[011] loading generates stacking faults more slowly, yet most of these defects persist upon unloading. This anisotropy arises from the significantly larger Schmid factors on the operative slip systems during [001] loading.

2. FCC–BCC phase transformation during shock loading also exhibits strong anisotropy. Under [001] loading, the transformation follows the Bain path and reverts to the FCC phase during unloading. In contrast, [011] loading leads to the FCC–BCC phase transition following the Pitsch orientation relationship.

The findings presented in this study establish a crucial theoretical foundation for subsequent dynamic experiments investigating Pb's shock-induced phase behavior. The techniques used in this study can be applied to investigating the dynamic processes of other materials of interest in this field, such as Al, Cu, and Fe. Our future work will systematically investigate the transformation pathways and underlying mechanisms associated with this unique orientation relationship.

Acknowledgments

This project was supported by the National Key R&D Program of China (Grant No. 2022YFA1004300) and the National Natural Science Foundation of China (Grant No. 12404004).

References

[1] Takahashi T, Mao H K and Bassett W 1969 *Science* **165** 1352
[2] Kuznetsov A, Dmitriev V, Dubrovinsky L, Prakapenka V and Weber H P 2002 *Solid State Commun.* **122** 125
[3] Sharma S M, Turneaure S J, Winey J M and Gupta Y M 2020 *Phys. Rev. Lett.* **124** 235701
[4] Krygier A, Powell P D, McNaney J M, Huntington C M, Prisbrey S T, Remington B A, Rudd R E, Swift D C, Wehrenberg C E, Arsenlis A, Park H S, Graham P, Gumbrell E, Hill M P, Comley A J and Rothman S D 2019 *Phys. Rev. Lett.* **123** 205701
[5] Chen Y, Ren G, Tang T, Li Q and Hu H 2016 *Shock Waves* **26** 221
[6] Antipov M V, Arinin V A, Georgievskaya A B, *et al.* 2017 *J. Dyn. Behav. Mater.* **3** 300
[7] Xiang M, Hu H and Chen J 2013 *J. Appl. Phys.* **113** 144312
[8] Xiang M Z, Hu H B and Chen J 2013 *Key Eng. Mater.* **577–578** 613
[9] Xiang M, Hu H, Chen J and Long Y 2013 *Model. Simul. Mater. Sci. Eng.* **21** 055005
[10] Wang K, Zhang F, He A and Wang P 2019 *J. Appl. Phys.* **125** 155107
[11] Mayer A E and Mayer P N 2020 *Int. J. Fract.* **222** 171
[12] Li G, Wang Y, Wang K, Xiang M and Chen J 2019 *J. Appl. Phys.* **126** 075902
[13] Wang K, Zhu W, Xiang M, Xu Y, Li G and Chen J 2018 *Model. Simul. Mater. Sci. Eng.* **27** 015001
[14] Liu A Y, Garca A, Cohen M L, Godwal B K and Jeanloz R 1991 *Phys. Rev. B* **43** 1795
[15] Cui S, Cai L, Feng W, Hu H, Wang C and Wang Y 2008 *Phys. Status Solidi B* **245** 53
[16] Cricchio F, Belonoshko A B, Burakovsky L, Preston D L and Ahuja R 2006 *Phys. Rev. B* **73** 140103
[17] Vohra Y K and Ruoff A L 1990 *Phys. Rev. B* **42** 8651
[18] Yu D and Scheffler M 2004 *Phys. Rev. B* **70** 155417
[19] Bombis C, Emundts A, Nowicki M and Bonzel H 2002 *Surf. Sci.* **511** 83
[20] Thompson A P, Swiler L P, Trott C R, Foiles S M and Tucker G J 2015 *J. Comput. Phys.* **285** 316
[21] Shapeev A V 2016 *Multiscale Model Sim.* **14** 1153
[22] Behler J and Parrinello M 2007 *Phys. Rev. Lett.* **98** 146401
[23] Bartók A P, Payne M C, Kondor R and Csányi G 2010 *Phys. Rev. Lett.* **104** 136403
[24] Chmiela S, Tkatchenko A, Sauceda H E, Poltavsky I, Schütt K T and Müller K R 2017 *Sci. Adv.* **3** e1603015
[25] Schütt K, Kindermans P J, Sauceda H E, Chmiela S, Tkatchenko A and Müller K R 2017 *Advances in Neural Information Processing Systems 30*, December 4–9, 2017, Long Beach, CA, USA, pp. 992
[26] Smith J S, Isayev O and Roitberg A E 2017 *Chem. Sci.* **8** 3192
[27] Han J, Zhang L, Car R and E W 2018 *Commun. Comput. Phys.* **23** 629
[28] Zhang L, Han J, Wang H, Saidi W A, Car R and E W 2018 *Advances in Neural Information Processing Systems 31 (NeurIPS 2018)*, December 3–8, 2018, Montréal, Canada
[29] Wood M A and Thompson A P 2017 arXiv:1702.07042 [physics.comp-ph]
[30] Kostiuchenko T S, Shapeev A V and Novikov I S 2024 *Chin. Phys. Lett.* **41** 066101
[31] Zhao K J and Song Z G 2025 *Chin. Phys. B* **34** 066101
[32] Xiong J H, Qi Z J, Liang K, Sun X, Sun Z P, Wang Q J, Chen L W, Wu G and Shen W 2023 *Chin. Phys. B* **32** 128101
[33] Yang F, Zeng Q, Chen B, Kang D, Zhang S, Wu J, Yu X and Dai J 2022 *Chin. Phys. Lett.* **39** 116301
[34] Hao M and Guan P 2023 *Chin. Phys. B* **32** 098401
[35] Li B, Yang Y, Fan Y, Zhu C, Liu S and Shi Z 2023 *Chin. Phys. Lett.* **40** 097402
[36] Zhang J, Chen G, Zhang C, Xu Y and Wang X 2025 *Chin. Phys. Lett.* **42** 056101
[37] Zhuang L, Ye Q, Pan D and Li X Z 2020 *Chin. Phys. Lett.* **37** 043101
[38] Qiu R, Zeng Q, Wang H, Kang D, Yu X and Dai J 2023 *Chin. Phys. Lett.* **40** 116301
[39] Chang X, Kang D, Chen B and Dai J 2025 *Chin. Phys. Lett.* **42** 053704
[40] Gao T, Zeng Q, Chen B, Kang D and Dai J 2024 *Acta Metall. Sinica* **60** 1439 (in Chinese)
[41] Zeng Q, Chen B, Kang D and Dai J 2023 *Acta Phys. Sin.* **72** 187102 (in Chinese)
[42] Liu L, Shi J, Song D and Miao C 2025 *Phys. Chem. Chem. Phys.* **27** 11684
[43] D'Souza J X, Hu S X, Mihaylov D I, Karasiev V V, Goncharov V N and Zhang S 2025 *Phys. Plasma* **32** 042701
[44] Pan S, Shi J, Liang Z, Liu C, Wang J, Wang Y, Wang H T, Xing D and Sun J 2024 *Phys. Rev. B* **110** 224101
[45] Zeng X, Xiao S, Chen Y, Li X, Wang K, Deng H, Zhu W and Hu W 2025 *Phys. B* **715** 417499
[46] Hou E, Wang X and Wang H *AIS Square Datasets* [2023-09]
[47] Mo P, Li C, Zhao D, Zhang Y, Shi M, Li J and Liu J 2022 *npj Comput. Mater.* **8** 107
[48] Wang H, Zhang L, Han J and E W 2018 *Comput. Phys. Commun.* **228** 178
[49] Chen M, Guo G and He L 2010 *J. Phys. Condens. Matter* **22** 445501
[50] Li P, Liu X, Chen M, Lin P, Ren X, Lin L, Yang C and He L 2016 *Comput. Mater. Sci* **112** 503
[51] Perdew J P, Burke K and Ernzerhof M 1996 *Phys. Rev. Lett.* **77** 3865
[52] Hamann D R 2013 *Phys. Rev. B* **88** 085117
[53] van Setten M, Giantomassi M, Bousquet E, Verstraete M, Hamann D, Gonze X and Rignanese G M 2018 *Comput. Phys. Commun.* **226** 39
[54] Tantardini C, Iliaš M, Giantomassi M, Kvashnin A G, Pershina V and Gonze X 2024 *Comput. Phys. Commun.* **295** 109002
[55] Marsh S P 1980 *LASL Shock Hugoniot Data* Vol. 5 (Berkeley: University of California Press)
[56] Li W, Hahn E N, Yao X, Germann T C and Zhang X 2019 *Acta Mater.* **167** 51
[57] Plimpton S 1995 *J. Comput. Phys.* **117** 1
[58] Larsen P M, Schmidt S and Schiøtz J 2016 *Model. Simul. Mater. Sci. Eng.* **24** 055007
[59] Stukowski A 2009 *Model. Simul. Mater. Sci. Eng.* **18** 015012
[60] Alippi P, Marcus P and Scheffler M 1997 *Phys. Rev. Lett.* **78** 3892
[61] Waitz T and Karnthaler H 1997 *Acta Mater.* **45** 837
[62] Pitsch W 1959 *Philos. Mag.* **4** 577